Communication



# Amorphous Co-NiB@NF as an Efficient Electrocatalyst for Urea Oxidation Reaction

Shuai Geng , Bo Hai , Heping Shi *

Posted Date: 17 June 2025

doi: 10.20944/preprints202506.1359.v1

Keywords: Co-NiB@NF; urea oxidation reaction; high efficiency

 doi:10.20944/preprints202506.1359.v1



*Communication*

# Amorphous Co-NiB@NF as an Efficient Electrocatalyst for Urea Oxidation Reaction

**Shuai Geng, Bo Hai and Heping Shi ***

College of science, Inner Mongolia Agricultural University, Hohhot, China

* Correspondence: hpshi2002@163.com Tel: 00-86-0471-4311386

**Abstract:** Transition metal-based catalysts designed for efficient urea oxidation reactions (UOR) are essential for hydrogen production via urea-assisted water electrolysis. A series of amorphous nickel cobalt boride catalysts supported on nickel foam were in-situ synthesized via a stepwise chemical deposition method (SCDM). The systematic investigation focused on the relationships between synthesis parameters (deposition cycles, reactant feed ratio), morphological characteristics, and UOR performance. Notably, the optimized Co-NiB@NF catalyst exhibits a porous hierarchical architecture composed of metallic nanoparticles encapsulated by surface-wrinkled nanosheets, forming abundant exposed active sites. Electrochemical measurements demonstrate that this catalyst requires a low cell potential of 1.29 V to achieve a current density of 10 mA $cm^{-2}$. Moreover, it maintains 83% of the initial current density after 10 hours of continuous electrolysis, highlighting its superior durability. The structural-property relationship revealed here provides valuable insights into the rational design of efficient amorphous boride catalysts for urea-assisted hydrogen production.

**Keywords:** Co-NiB@NF; urea oxidation reaction; high efficiency

## 1. Introduction

Hydrogen, as a clean energy carrier, demonstrates significant potential for mitigating large-scale greenhouse gas emissions and environmental pollution associated with fossil fuels [1]. Among diverse hydrogen production technologies, electrochemical water splitting is considered the most promising pathway for "green" hydrogen generation, primarily due to its direct integration with intermittent renewable energy sources (e.g., wind and solar power). Nevertheless, the high thermodynamic potential of the anodic oxygen evolution reaction (OER, 1.23 V vs. RHE) and its sluggish kinetics remain critical bottlenecks impeding its industrial implementation [2].

Using urea as an anodic sacrificial reagent and replacing the OER with the more thermodynamically favorable urea oxidation reaction (UOR, 0.37 V vs. RHE) not only reduces energy consumption but also provides a synergistic solution for nitrogen-containing wastewater treatment [3]. Nevertheless, UOR involves a complex six-electron transfer mechanism and suffers from sluggish kinetics, underscoring the urgent need for highly active and robust electrocatalysts. In alkaline electrolyte, the overall urea electrolysis reaction is as follows:

$$\text{Anode:} \quad CO(NH_2)_2 + 6OH^- \rightarrow N_2 + CO_2 + 5H_2O + 6e^- \tag{1}$$

$$\text{Aathode:} \quad 6H_2O + 6e^- \rightarrow 3H_2 + 6OH^- \tag{2}$$

$$\text{Overall:} \quad CO(NH_2)_2 + H_2O \rightarrow N_2 + CO_2 + H_2 \tag{3}$$

To date, various binary and ternary transition-metal boride (TMB) catalysts—such as Co-Zn-B and W-Fe-Ni-B—have demonstrated exceptional UOR performance. This stems from the tunable combinations of transition metal ions, the metalloid character of boron, and its electron-deficient structure, which collectively enable remarkable flexibility in electronic structure engineering [4,5]. Most transition metal boride-based catalysts synthesized currently are in amorphous form; compared to crystalline counterparts, they exhibit more flexible structures and higher defect density [6].

 doi:10.20944/preprints202506.1359.v1



Existing literature has shown that amorphous nickel cobalt borides possess high catalytic activity toward OER, yet their performance in UOR remains largely unexplored. Additionally, conventional chemical deposition methods for synthesizing amorphous borides often suffer from issues like low efficiency, uneven loading, and difficulty in controlling loading amounts. To address these challenges, this work modifies the chemical deposition approach and elucidates the correlations among synthesis conditions (deposition cycles, feed ratio), product morphology, and UOR performance.

In this study, an amorphous cobalt-doped nickel boride catalyst (Co-NiB@NF) supported on nickel foam was in situ synthesized via the stepwise chemical deposition method (SCDM). The as-prepared catalyst features metal boride nanoparticles encapsulated by layered oxides/hydroxides. It delivers a potential of only 1.29 V at a current density of 10 $mA \cdot cm^{-2}$ and 1.41 V at 100 $mA \cdot cm^{-2}$, with 83% current retention over 10 hours, demonstrating exceptional catalytic activity and stability. This facile synthesis strategy for amorphous transition-metal boride (TMB) catalysts provides an effective pathway for the development of high-performance urea oxidation reaction (UOR) electrocatalysts.

## 2. Materials and Methods

### *2.1. Preparation of Ni–Co Boride*

(1) Preparation of Deposition Solutions

Solution A was prepared by dissolving $NiSO_4 \cdot 6H_2O$ and $CoSO_4 \cdot 7H_2O$ in deionized water such that the total metal ion concentration was 0.20 M. Sodium succinate (0.20 M) was added as a complexing agent.

Solution B was prepared by dissolving NaOH (0.10 M) and $NaBH_4$ (0.60 M) in deionized water.

(2) Stepwise Deposition Procedure

In each deposition cycle, 10 mL of Solution A and 10 mL of Solution B were placed in separate beakers. Nickel foam (NF) substrates were first immersed in Solution A for 1 min, then immediately transferred to Solution B for 1 min, and finally rinsed thoroughly with deionized water. This sequence constitutes one deposition cycle.

(3) Tailoring Ni/Co Ratio and Deposition Number

By varying the Ni: Co feed ratio in Solution A and the number of deposition cycles, a series of Ni–Co boride catalysts were synthesized. For example, when the Ni/Co molar ratio was set to 9:1 and the deposition was repeated 11 times, the resulting sample was denoted as Co-NiB@NF.

### *2.2. Preparation of $Ni_9Co_1$-LDH@NF*

The total concentration of $NiSO_4 \cdot 6H_2O$ and $CoSO_4 \cdot 7H_2O$ in the solution was set to 0.20 M with a Ni/Co molar ratio of 9:1, and 0.09 M urea was used as the precipitating agent. Forty milliliters of this solution were placed together with NF into a 50 mL beaker and heated in an 80 °C water bath for 7 h to obtain $Ni_9Co_1$-LDH@NF.

The working electrode was prepared by cutting the as-synthesized catalyst into a 1×1.5 $cm^2$ piece, which was then fixed with a platinum plate electrode clip to ensure an immersed area of 1 $cm^2$ in the electrolyte.

### *2.3. Catalytic Characterization*

The catalyst samples were characterized by powder X-ray diffraction (XRD, Tongda TD-3700 , Cu Ka radiation), scanning electron microscopy (SEM, TH4000 Hitachi ), transmission electron microscopy (TEM, Tecnai F20 ), and X-ray photoelectron spectroscopy (XPS, ESCALAB 250Xi, Al Ka-rays source). In the XPS measurements, all the binding energies (BE) were calibrated using the C 1s peak (at 284.8 eV) of the adventitious carbon as an internal standard. The curve fitting was performed using Thermo Avantage software. *The samples required for XRD, XPS, and TEM characterizations were powders obtained by ultrasonically treating the catalyst to peel it off from the NF substrate. *

 doi:10.20944/preprints202506.1359.v1



*2.4. Electrochemical Measurement*

Electrochemical measurements were performed in a standard three-electrode configuration using a CHI 660E electrochemical analyzer. The electrochemical cell comprised a catalytic electrode as the working electrode, a Pt sheet counter electrode, and an Ag/AgCl (saturated KCl) reference electrode. Potentials measured versus Ag/AgCl were referenced to the reversible hydrogen electrode (RHE) by adding a value of (0.197 + 0.059pH) V. A mixed solution of 1 M KOH and 0.33 M urea was used as the electrolyte.

Catalyst samples were electrochemically activated via potential cycling at a sweep rate of 20 mV/s for 20 cycles. All polarization curves were recorded at a sweep rate of 20 mV/s. Electrochemical impedance spectroscopy (EIS) measurements were conducted in the same three-electrode system at 1.29 V (vs. RHE). Impedance spectra were collected over a frequency range of 0.01 Hz to 100 kHz with a 10 mV amplitude.

The electrochemical active surface area (ECSA) was estimated by measuring the double-layer capacitance of the system via cyclic voltammetry (CV). A series of CV tests were conducted within the potential window of 1.064 to 1.164 V (vs. RHE) at different scan rates (20, 40, 60, 80, 100 mV $s^{-1}$, etc.). Subsequently, a linear plot was obtained by establishing the relationship between the difference of anodic and cathodic currents ($i_a$ - $ic$) at 1.114 V (vs. RHE) and the scan rate. The double-layer capacitance ($C_{dl}$) was half of the slope value of the fitted line. The ECSA is calculated based on the equation ECSA=$C_{dl}$/Cs, where Cs represents the specific capacitance of a smooth planar electrode (typically reported as 0.04 mF $cm^{-2}$ in previous studies) [7]。

All tests were conducted without IR correction. The working electrode was prepared by cutting the as-synthesized catalyst into a 1×1.5 $cm^2$ piece, which was fixed with a platinum plate electrode clip to ensure an immersed area of 1 $cm^2$ in the electrolyte.

## 3. Results and Discussion

*3.1. Morphology and Structure*

The amorphous Co-NiB@NF catalyst was synthesized via a stepwise chemical deposition method under ambient conditions (room temperature, non-oxygen-isolated atmosphere). Compared with conventional single-step deposition, this stepwise strategy exhibits higher efficiency and better control over catalyst loading.

As shown in Figure 1a, Co-NiB@NF exhibits a hierarchical architecture, where primary particles (~100 nm in diameter) are decorated with irregularly grown crumpled nanosheets (~100 nm in depth). High-resolution TEM (Figure 1b) reveals discontinuous lattice fringes with short-range ordered but long-range disordered atomic arrangements, characteristic of amorphous materials. Fourier transform analysis of locally ordered regions yielded a lattice spacing of 2.64 Å, indexed to the (101) plane of nickel hydroxide (PDF#01-089-7111). EDS elemental mapping (Figure 1c) confirmed the coexistence of Ni, Co, B, and O, evidencing successful multi-element doping while indicating partial oxidation caused by oxygen exposure during synthesis and storage. The XRD pattern is shown in Figure 3, displaying significantly broadened diffraction peaks at around 2θ=20° and 45°. These broad peaks are characteristic of metal borides, indicating the amorphous structure of the Co-NiB@NF catalyst. The weak diffraction peaks of Ni/Co oxides appearing at approximately 2θ=36° and 60° suggest that surface oxidation of the catalyst occurred during synthesis and storage [8]. During synthesis, Co-NiB@NF initially deposited as reduced metallic boride nanoparticles on the NF substrate. Subsequent self-reconstruction under aerobic conditions generated an amorphous boride-containing oxide/hydroxide overlayer encapsulating the nanocrystalline metallic cores. These boron-derived species act as stabilizing agents, protecting the metallic cores from oxidative degradation during UOR catalysis [16].

 doi:10.20944/preprints202506.1359.v1



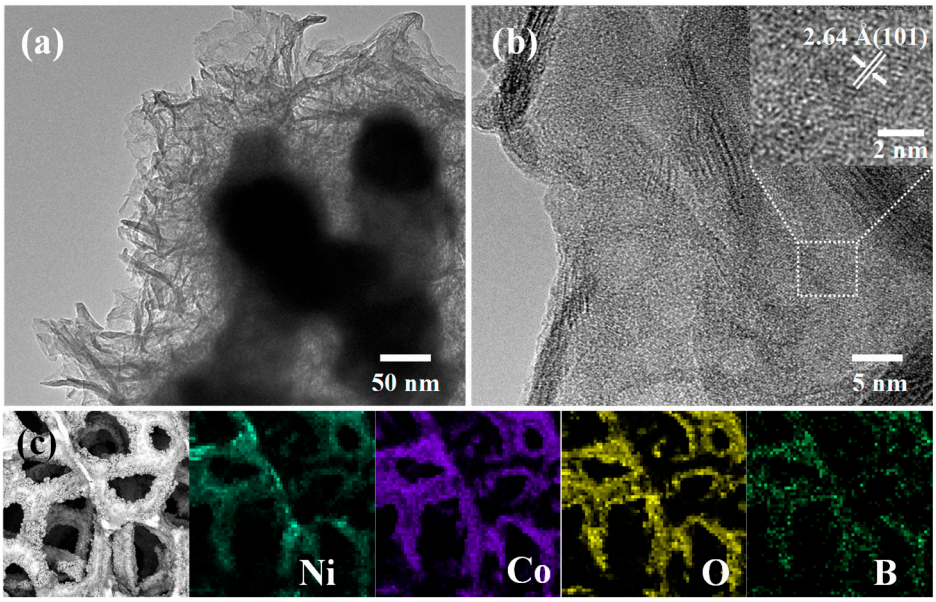


**Figure 1.** (a) (b) TEM were images of Co-NiB@NF, (c) EDS image of Co-NiB@NF.

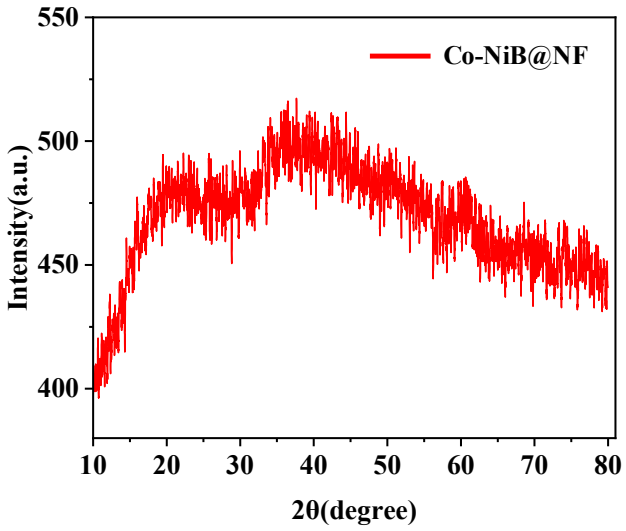


**Figure 2.** XRD pattern of Co-NiB@NF.

XPS was used to analyze the surface chemical states of the Ni-B@NF and Co-NiB@NF catalysts (Figure 3). In the XPS spectrum of Co-NiB@NF, elements such as Ni, Co, B, and O were detected, consistent with the EDS results. The Ni/Co ratio was found to be 8.5: 1.5, slightly higher than the 9:1 molar ratio used during synthesis. In the Ni 2p spectrum, two prominent peaks at 855.33 eV and 856.33 eV were assigned to $Ni^{2+}$ and $Ni^{3+}$ oxidation states, respectively, while a weaker peak at 852.53 eV was assigned to $Ni^{0}$ (Figure 3a). Similarly, in the Co 2p spectrum (Figure 3b), characteristic peaks of $Co^{2+}$ and $Co^{3+}$ were detected, along with a weaker $Co^{0}$ peak[9]. The B1s spectrum shows a small amount of M-B bonds and a large amount of B-O species (Figure 3c). The high-valent nickel and cobalt originate from atmospheric exposure during the preparation and storage process, leading to the formation of Ni/Co oxides and hydroxides on the surface of Co-NiB@NF, although a small amount of unoxidized Ni/Co metals remain [10]. In the B1s spectrum, the $B^{0}$ characteristic peak of Co-NiB@NF at 189.59 eV shifts negatively by 0.5 eV compared to the $B^{0}$ peak of Ni-B@NF at 189.09 eV, confirming the successful synthesis of the Co-NiB ternary boride [11]. The O 1s spectrum is shown in Figure 3d, indicating that oxygen elements on the surface of Co-NiB@NF are predominantly

 doi:10.20944/preprints202506.1359.v1



hydroxyl oxygen, with a small amount of lattice oxygen. The high content of oxygen vacancy species suggests that the amorphous boride possesses a rich defect structure. After electrochemical testing, the B 1s signal in Co-NiB@NF completely disappeared, accompanied by a significant increase in $M^{3+}$ content, indicating that the catalyst underwent further surface reconstruction during the test. The changes in XPS spectra demonstrate that the newly formed oxide layer masked the signals of boron-oxygen species [12,13].

The ubiquitous presence of oxide/hydroxide layers, structural defects, and zero-valent metal signatures on Co-NiB@NF are consistent with literature descriptions of amorphous metal borides possessing a "oxide/hydroxide shell encapsulating a metal-boride core." [14]

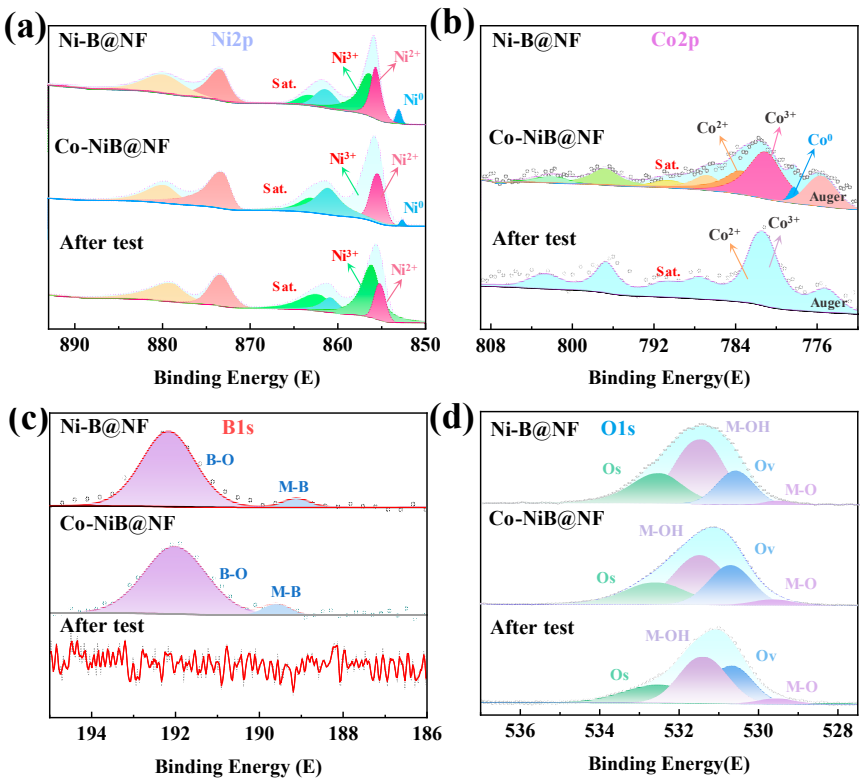


**Figure 3.** Ni2p, Co2p, B1s and O1s XPS spectrums of Ni-B@NF, Co-NiB@NF and activated Co-NiB@NF.

During the in-situ synthesis of amorphous Co-NiB@NF catalysts via the SCDM, deposition parameters—specifically the number of deposition cycles and Co precursor ratio—directly governed the morphological evolution of the catalyst layer on the NF substrate. Figure 4 shows SEM images of Co-NiB@NF samples prepared with varying numbers of deposition cycles. As the number of deposition cycles increases, Co-NiB@NF-9 (Figure 4a), Co-NiB@NF-11 (Figure 4b), and Co-NiB@NF-13 (Figure 4c) exhibit significant morphological differences. These morphological changes can be attributed to the layer-by-layer assembly of catalyst particles during the SCDM process. Tests of catalyst loading and performance (Figure S1) indicate that increasing the number of deposition cycles leads to higher catalyst loading (When the number of deposition cycles is 11, the loading amount of Co-NiB@NF is 2.75 $mg \cdot cm^{-2}$). As a result, Co-NiB@NF-11 exhibits higher performance than Co-NiB@NF-9; however, Co-NiB@NF-13, despite having the highest loading, shows a decline in performance. These results suggest that when the number of deposition cycles is relatively low, the catalyst loading is insufficient. Conversely, when the number of deposition cycles is excessively high, the deposited layer becomes too thick, which adversely affects mass transfer. Thus, an optimal number of deposition cycles yields a porous deposited layer with an appropriate catalyst loading on the NF surface.

 doi:10.20944/preprints202506.1359.v1



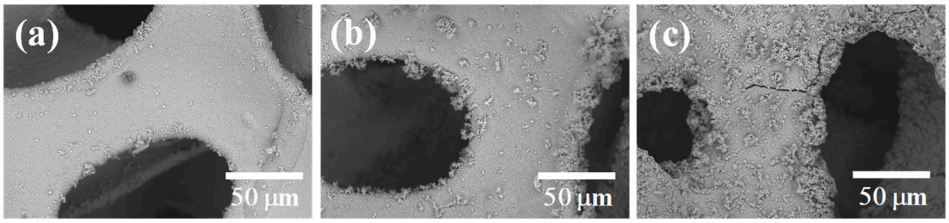


**Figure 4.** Panels a, b, and c are SEM images of Co–B@NF after 9, 11, and 13 deposition cycles.

The experimental results indicate that varying the Co precursor ratio has a pronounced influence on the morphology of these amorphous Ni-Co-B catalysts—an effect that has been rarely reported in the literature. Figure 5 presents SEM images corresponding to different Co precursor ratios, revealing a strong correlation between the precursor ratio and the resulting catalyst morphology. As the proportion of $Co^{2+}$ increases (from Ni-B@NF in Figure 5a to Co-B@NF in Figure 5d), the catalyst morphology changes significantly and systematically. These observations suggest that the presence of $Co^{2+}$ during the deposition process promotes aggregation of the deposited material, with this tendency becoming stronger at higher $Co^{2+}$ ratios. Such aggregation directly reduces the number of electrochemically active sites on the catalyst surface, thereby impairing its performance in the UOR (Figure S2).

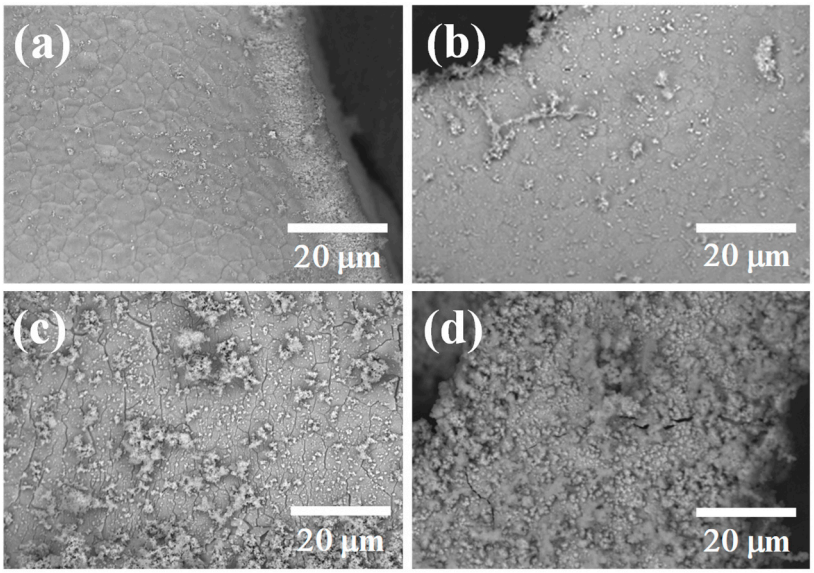


**Figure 5.** SEM images of catalysts after 11 deposition cycles with varying Co feed ratios: (a) Ni-B@NF; (b) Co-NiB@NF; (c) $Ni_5$-$Co_5$@NF; (d) Co-B@NF.

*3.2. UOR Performance*

Figure 6a shows that the Co-NiB@NF catalyst exhibits optimal UOR catalytic performance, achieving a current density of 10 mA·cm$^{-2}$ at only 1.29 V, and reaching 100 mA·cm$^{-2}$ at 1.41 V. Under identical test parameters, when evaluating the OER performance of this catalyst in 1 M KOH, a potential of 1.77 V is required to achieve a current density of 100 mA·cm$^{-2}$ (Figure 7a). Furthermore, in a 10-hour chronoamperometry test, the current density shows only a small decrease (Figure 7c), indicating excellent stability. This performance is comparable to most previously reported transition metal-based catalysts (Table 1).

When compared with the monometallic catalysts Ni-B@NF and Co-B@NF, as well as the bimetallic hydroxide $Ni_9Co_1$-LDH@NF, Co-NiB@NF demonstrates superior performance. Its Tafel slope is 63.07 mV dec$^{-1}$ (Figure 6b), which is higher than that of Ni-B@NF (43.97 mV dec$^{-1}$), indicating

 doi:10.20944/preprints202506.1359.v1



that Co doping does not fully exert a positive effect. The electrochemical impedance spectroscopy (EIS) in Figure 6c and the double-layer capacitance measurements in Figures S3 and 6d show that the introduction of a small amount of Co not only significantly reduces the charge-transfer resistance of Co-NiB@NF but also decreases its electrochemical active surface area.

Consequently, Co-NiB@NF achieves higher current densities and lower overpotentials than Ni-B@NF. This can be attributed to the Co-induced improvement in charge transfer, which enhances the catalyst's intrinsic activity. The higher Tafel slope, however, results from Co doping altering the catalyst morphology and reducing the number of active sites. Compared with $Ni_9Co_1$-LDH@NF, Co-NiB@NF exhibits a higher current density and a lower Tafel slope, highlighting the advantages brought about by its amorphous structure and B-element doping.

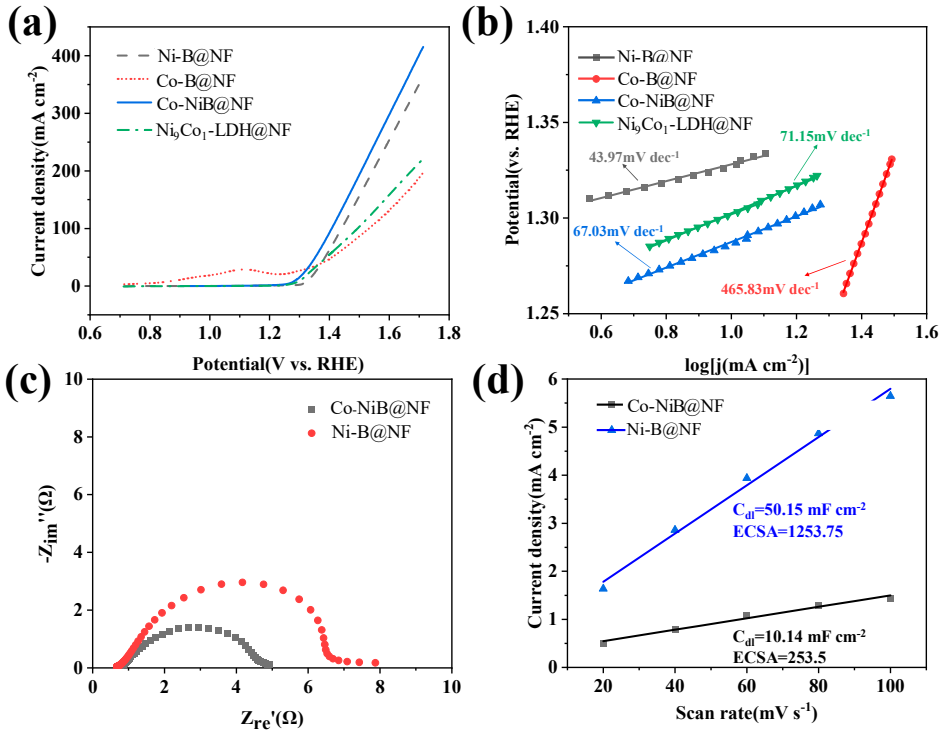


**Figure 6.** Electrocatalytic UOR performance (a) LSV curves; (b) corresponding Tafel slopes; (c) EIS of the samples, (d) Estimation of the $C_{dl}$ values and ECSA.

Recent theoretical studies on Ni-B electrocatalysts indicate that the original Ni-BOx species undergo self-reconstruction into γ-NiOOH to catalyze UOR. This γ-NiOOH phase is thermodynamically favored under oxidative conditions and has been identified as the primary active species for urea oxidation reaction (UOR) catalysis. However, the catalytic cycle on NiOOH involves energetically demanding steps, such as the formation of oxygenated intermediates (*OOH or *OH) on its surface, which kinetically limits the overall UOR kinetics [15]. In other words, while NiOOH represents the stable oxidized Ni phase, the adsorption and conversion of urea-derived intermediates on this surface may encounter kinetic barriers.

The electrochemical behavior of the catalyst was observed via CV measurements (Figure 7b): compared with Ni-B@NF, the generation potential of NiIII/Ni II in Co-NiB@NF exhibited a negative shift of 25 mV, indicating that amorphous Co-NiB@NF accelerates structural self-reconstruction during UOR. This can be attributed to doped Co cations reducing the structural self-transformation energy, thereby lowering the energy barrier for UOR. Additionally, d-d orbital delocalization between Ni and Co decreases the d-band center of Ni, balancing the adsorption energy of UOR intermediates on the NiOOH surface, which endows Co-NiB@NF with higher UOR activity than Ni-B@NF. The experimental results are consistent with these theoretical predictions: introducing a small

 doi:10.20944/preprints202506.1359.v1



amount of Co into the Ni-B@NF catalyst significantly enhances its electrocatalytic performance [14,16].

Based on the above analysis, we conclude that the hydroxide form of $Ni^{3+}$ serves as the main active center for OER, while Co reduces the energy barrier for forming NiIII intermediates and optimizes the adsorption energy of UOR intermediate products.

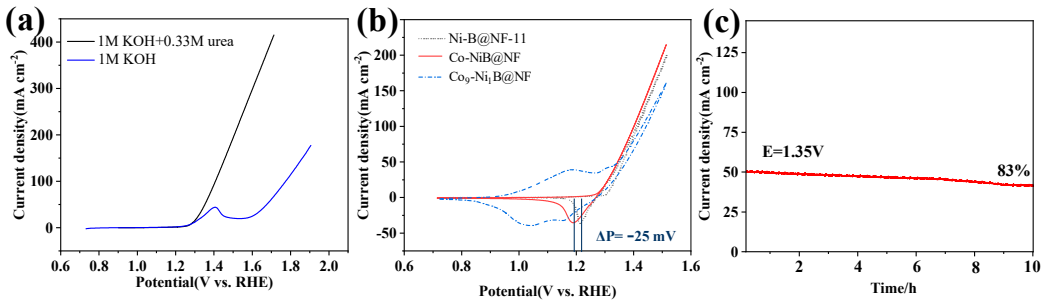


**Figure 7.** (a) Comparison of LSV curves of Co-NiB@NF for UOR and OER; (b) CV curves; (c) I-t of Co-NiB@NF.

**Table 1.** Comparison of catalyst performance.

| Material/substrate | Electrolyt | Potential (V vs. RHE) @ (mA $cm^{-2}$) | Reference |
|---|---|---|---|
| Co-NiB@NF | 1MKOH+0.33M urea | 1.29@10 | This work |
| aFe-NiB | 1MKOH+0.5M urea | 1.29@10 | [16] |
| Mn-$Ni(OH)_2$/CP | 1MKOH+0.33M urea | 1.33@10 | [17] |
| $NiMoS_2$/NF | 1MKOH+0.33M urea | 1.39@10 | [18] |
| Ru-$Ni_3N$@NC | 1MKOH+0.33M urea | 1.36@10 | [19] |
| O-NiMoP/NF | 1MKOH+0.5M urea | 1.41@100 | [20] |
| Ni/NiMoN | 1MKOH+0.5M urea | 1.39@100 | [21] |
| W-NT@NF-3 | 1MKOH+0.33M urea | 1.43@100 | [22] |

## 4. Conclusion

A simple staged SCDM was used to efficiently deposit the amorphous Co-NiB@NF ternary boride onto a nickel foam substrate. The catalyst achieved a current density of 10 mA·$cm^{-2}$ at only 1.29 V, and a current density of 100 mA·$cm^{-2}$ at 1.41 V. In a 10-hour constant potential test, the current density retention reached 83%. In summary, the improved catalytic performance of the NiCoB-based composite is attributed to the synergistic optimization of its electronic structure and microstructure achieved during synthesis. The electron-donor effect of boron atoms toward cobalt establishes directed charge-transfer pathways, which effectively lower the d-band center of the Ni active sites and promote the formation of $Ni^{3+}$ active species. Meanwhile, the metallic NiCoB core and its in situ reconstructed amorphous hydroxide shell form a unique core–shell architecture: the high electrical conductivity of the core ensures rapid charge transport, while the shell's wrinkled, sheet-like morphology not only exposes abundant active sites but also significantly enhances reactant mass transport and bubble detachment through its interwoven porous framework. By integrating compositional design with structural control, this study demonstrates the practical potential of transition metal borides in the UOR system and provides a valuable strategy for developing non-precious metal electrocatalysts that exhibit both high activity and high stability.

**Supplementary Materials:** The following supporting information can be downloaded at the website of this paper posted on Preprints.org.

**Author Contributions:** Shuai Geng: Writing original draft, Funding acquisition, Formal analysis, Conceptualization. Bo Hai: Methodology. Heping Shi: Supervision.

 doi:10.20944/preprints202506.1359.v1



**Funding:** This work is supported by the Research on Key Technologies for Ecological Remediation and Management of Heavy Metal Compound Pollution in Grassland Soils of Inner Mongolia Plateau, Project No. 2024KJHZ0018, Key R&D and Achievement Transformation Program of Inner Mongolia Autonomous Region. and Study on the Sources Identification and Adsorption-Degradation Mechanism of Antibiotics in Soil and Water of Hetao Irrigation Area, Inner Mongolia, Project No. 2024LHMS04017, Natural Science Foundation of Inner Mongolia.

**Data Availability Statement:** Data are contained within the article.

**Acknowledgments:** Gratitude to Teacher Heping Shi and Teacher Bo Hai for their help.

**Conflicts of Interest:** The authors declare that they have no known competing financial interests or personal relationships that could have appeared to influence the work reported in this paper.

**Declaration of Generative AI and AI-Assisted Technologies in the Writing Process:** During the preparation of this work the authors used Chat GPT to polish the English. After using this tool, the authors reviewed and edited the content as needed and took full responsibility for the content of the publication.

## References

1. Oliveira, A. M.; Beswick, R. R.; Yan, Y. A Green Hydrogen Economy for a Renewable Energy Society. *Curr. Opin. Chem. Eng.* **2021**, *33*, 100701., https://doi.org/10.1016/j.coche.2021.100701.
2. Hai, B.; Huang, W.; Li, J. Promotion Effects of Pr-Doped $CeO_2$·$H_2O$ to Pt Catalysts toward Alcohol Electrooxidation Reaction. *Mater. Lett.* **2023**, *349*, 134796, https://doi.org/10.1016/j.matlet.2023.134796.
3. Singh, R. K.; Rajavelu, K.; Montag, M.; et al. Advances in Catalytic Electrooxidation of Urea: A Review. *Energy Technol.* **2021**, *9*, 2100017, https://doi.org/10.1002/ente.202100017.
4. Chen, H.; Zou, X. Intermetallic Borides: Structures, Synthesis and Applications in Electrocatalysis. Inorg. *Chem. Front.* **2020**, *7*, 2248–2264, https://doi.org/10.1039/D0QI00146E.
5. Quílez-Bermejo, J.; García-Dalí, S.; Karthik, R.; et al. Zinc Doping Enhances the Electrocatalytic Properties of Cobalt Borides for the Hydrogen Evolution Reaction. *Front. Energy Res.* **2022**, *10*, 901395, https://doi.org/10.3389/fenrg.2022.901395.
6. Li, L.; Shao, Q.; Huang, X. Amorphous Oxide Nanostructures for Advanced Electrocatalysis. *Chem. Eur. J.* **2020**, *26*, 3943–3960, https://doi.org/10.1002/chem.201903206.
7. Guo, F.; Wu, Y.; Chen, H.; et al. High-Performance Oxygen Evolution Electrocatalysis by Boronized Metal Sheets with Self-Functionalized Surfaces. *Energy Environ. Sci.* **2019**, *12*, 684–692. https://doi.org/10.1039/C8EE03405B
8. Ma, Y.; Dong, J.; Yang, X.; et al. Hydrogelator as Growth-Controlling Agent for Enhancing the Catalytic Activity of NiB Amorphous Alloy Catalyst. *Res. Chem. Intermed.* **2018**, *44*, 7861–7872. https://doi.org/10.1007/s11164-018-3591-x
9. Zhou, T.; Jagadeesan, S. N.; Zhang, L.; et al. Enhanced Urea Oxidation Electrocatalytic Activity by Synergistic Cobalt and Nickel Mixed Oxides. *J. Phys. Chem. Lett.* **2023**, *15*, 81–89, https://doi.org/10.1021/acs.jpclett.3c03257.
10. Fang, W.; Zhu, Z.; Yu, J.; et al. First Principles Study on High-Efficient Overall Water Splitting by Anchoring Cobalt Boride with Transition Metal Atoms. *Int. J. Hydrogen Energy* **2024**, *53*, 1310–1322. https://doi.org/10.1016/j.ijhydene.2023.11.347
11. Tian, Z.; Zhou, K.; Xie, M.; et al. Self-Supported Nickel Iron Selenide@Nickel Cobalt Boride Core-Shell Nanosheets Electrode for Asymmetric Supercapacitors. *Chem. Eng. J.* **2022**, *447*, 137495. https://doi.org/10.1016/j.cej.2022.137495
12. Jamadar, A. S.; Sutar, R. B.; Patil, S.; et al. Attaining High-Rate Hydrogen Evolution via SILAR Deposited Bimetallic Nickel Cobalt Boride Electrode: Exploring the Influence of Ni to Co Ratio. *Int. J. Hydrogen Energy* **2024**, *85*, 661–672. https://doi.org/10.1016/j.ijhydene.2024.08.426
13. Xu, N.; Cao, G.; Chen, Z.; et al. Cobalt Nickel Boride as an Active Electrocatalyst for Water Splitting. J. Mater. Chem. A **2017**, *5*, 12379–12384. https://doi.org/10.1039/C7TA02644G

 doi:10.20944/preprints202506.1359.v1




14. Sivagurunathan, A. T.; Seenivasan, S.; Kavinkumar, T.; et al. Phosphorus Doping of Nickel–Cobalt Boride to Produce a Metal–Metalloid–Nonmetal Electrocatalyst for Improved Overall Water Splitting. *J. Mater. Chem. A* **2024**, *12*, 4643–4655, https://doi.org/10.1039/D3TA07382C.
15. Li, R.; Hu, B.; Yu, T.; et al. Insights into Correlation among Surface-Structure-Activity of Cobalt-Derived Pre-Catalyst for Oxygen Evolution Reaction. *Adv. Sci.* **2020**, *7*, 1902830, https://doi.org/10.1002/advs.201902830.
16. Chen, Z.; Zheng, R.; Zou, H.; et al. Amorphous Iron-Doped Nickel Boride with Facilitated Structural Reconstruction and Dual Active Sites for Efficient Urea Electrooxidation. *Chem. Eng. J.* **2023**, *465*, 142684, https://doi.org/10.1016/j.cej.2023.142684
17. Liu, X.; Qin, H.; Ye, Z.; et al. Interconnected Mn-Doped Ni(OH)2 Nanosheet Layer for Bifunctional Urea Oxidation and Hydrogen Evolution: The Relation between Current Drop and Urea Concentration during the Long-Term Operation. *ACS ES&T Eng.* **2022**, *2*, 853–862, https://doi.org/10.1021/acsestengg.1c00400.
18. Sreenivasulu, M.; Shetti, R. S.; Mathi, S.; et al. Ni-Tethered MoS2: In-Situ Fast Reduction Synthesis as an Ultra-Durable and Highly Active Electrocatalyst for Water Splitting and Urea Oxidation. *Mater. Today Sustain.* **2024**, *26*, 100782, https://doi.org/10.1016/j.mtsust.2024.100782.
19. Liu, Y.; Zheng, D.; Zhao, Y.; et al. Ru-Doped 3D Porous Ni3N Sphere as Efficient Bi-Functional Electrocatalysts toward Urea Assisted Water-Splitting. *Int. J. Hydrogen Energy* **2022**, *47*, 25081–25089, https://doi.org/10.1016/j.ijhydene.2022.05.268.
20. Jiang, H.; Sun, M.; Wu, S.; et al. Oxygen-Incorporated NiMoP Nanotube Arrays as Efficient Bifunctional Electrocatalysts for Urea-Assisted Energy-Saving Hydrogen Production in Alkaline Electrolyte. *Adv. Funct. Mater.* **2021**, *31*, 2104951, https://doi.org/10.1002/adfm.202104951.
21. Fan, Y.; Gu, Y.; Wang, D.; et al. Hollow NiMo-Based Nitride Heterojunction with Super-Hydrophilic/Aerophobic Surface for Efficient Urea-Assisted Hydrogen Production. *J. Energy Chem.* **2024**, *95*, 428–439, https://doi.org/10.1016/j.jechem.2024.04.002.
22. Liu, M.; Zou, W.; Qiu, S.; et al. Active Site Tailoring of Ni-Based Coordination Polymers for High-Efficiency Dual-Functional HER and UOR Catalysis. *Adv. Funct. Mater.* **2024**, *34*, 2310155, https://doi.org/10.1002/adfm.202310155.